Tellus (1997), 49B, 216–230
Printed in UK – all rights reserved

TELLUS
ISSN 0280–6509

On monitoring the atmospheric greenhouse effect from space

By A. K. INAMDAR* and V. RAMANATHAN, *Center for Atmospheric Sciences, Scripps Institution of Oceanography, UCSD, La Jolla, CA 92093, USA*

(Manuscript received 23 October 1995; in final form 14 October 1996)

ABSTRACT

We propose an analysis technique for monitoring the planetary greenhouse effect from space. 2 quantities are used as a measure of the atmospheric greenhouse effect: (1) G_a, which is the reduction in the clear sky outgoing longwave radiation (OLR) due to the atmosphere; it is the radiative heating of the surface-atmosphere column; (2) G_a^*, which is the back radiation from the atmosphere to the surface; it is the radiative heating of the surface by the atmosphere. G_a is obtained from satellite observations of OLR and surface temperature. Here, we develop a technique to obtain G_a^* from a combination of OLR (broadband and window channel), surface temperature, column water vapor amount and near-surface air temperature. The difference, $G_a - G_a^*$, yields the net radiative cooling of the atmospheric column. While the technique is applicable for any radiometric observations, it is demonstrated here for the proposed cloud and the earth's radiant energy systems (CERES). CERES will have in addition to the broadband channel (4 to 200 μm), a channel in the atmospheric window (8–12 μm) to provide continuous radiation flux data. The potential benefits of the window channel in estimating the surface downward longwave flux, as also in addressing the water vapor feedback and continuum-related studies are explored in this paper. The success of the method in unravelling the water vapor — radiative interactions is illustrated by 2 case studies using ship and satellite data for the 1985 to 1990 period: (a) the seasonal and latitudinal variation in the northern tropical oceans; (b) seasonal to inter-annual variations averaged over the entire tropical (30° N to 30° S) pacific ocean. In both instances, the column greenhouse effect (G_a) varies significantly on seasonal and inter annual time scales and is larger in the warmer months. Furthermore, variations in G_a^* exceed those in G_a, such that the atmospheric cooling increases in the warmer, moist atmosphere. The water vapor continuum plays a significant role in the tropical variations of G_a^* and tropospheric radiative cooling.

1. Introduction

Two measures are used to quantify the magnitude of the atmospheric greenhouse effect: G_a and G_a^* (Table 1). G_a is the reduction in the outgoing longwave radiation (OLR) due to the presence of the atmosphere and G_a^* is the downward longwave radiation at the surface. G_a is a measure of the vertically integrated atmospheric greenhouse effect from the surface to the top-of-the-atmosphere and enters directly into the governing equations of climate (Dutton, 1995). It can be estimated from satellite measurements of OLR, data for surface temperature and emissivity (Table 1). As shown in Raval and Ramanathan (1989) and Stephens and Greenwald (1991), latitudinal and seasonal variations in G_a can be used to understand the water vapor greenhouse effect and its variations. Global mean variations in G_a on time scales ranging from months to years can be used to understand the role of water vapor feedback in climate changes.

* Corresponding author.
e-mail: anand@fiji.ucsd.edu or ram@ucsd.edu

Table 1. *Table of symbols and definitions*

Symbol	Description	Comments and definition
T_s	surface temperature	K
T_a	atmospheric temperature	subscript indicates the pressure level
w_{tot}	total column precipitable water	g cm^{-2}
$^*F^+_\infty$	longwave flux at the top of atmosphere	W m^{-2}
G^*_a	downward longwave flux at the surface	W m^{-2}
F^+_0	surface black body emission	$\approx \sigma T_s^4$
f^+_∞	normalised F^+_∞	$f^+_\infty = F^+_\infty / F^+_0$
g^*_a	normalised G^*_a	$g^*_a = G^*_a / F^+_0$
G_a	clear-sky greenhouse effect of the atmosphere	$G_a = F^+_0 - F^+_\infty$
g_a	normalised G_a	$g_a = G_a / F^+_0 = 1 - f^+_\infty$
I^-_0	downwelling radiance in the 500 to 2000 cm^{-1} range	W m^{-2} sterad^{-1}
ε	surface emissivity	

* The second subscripts "win" and "nw" for any flux parameter denote the corresponding quantities integrated over the window (8–12 μm) and non-window spectral intervals respectively.

The next important component is G^*_a, the downward longwave flux at the surface. It has been suggested (Minschwaner and McElroy, 1992) that the downward longwave flux may be adopted as an alternate measure of the strength of the greenhouse effect. Increase in G^*_a contributes to a direct radiative heating of the surface, while the difference, $G_a - G^*_a$, denotes the radiative forcing of the atmosphere, i.e.,

$$\Delta R_L(SA) = \Delta G_a$$

$$\Delta R_L(S) = \Delta G^*_a$$

$$AR_L(A) = \Delta G_a - \Delta G^*_a$$

where SA is surface atmospheric column; S is surface and A is atmosphere (vertically integrated from $z = 0$ km to ∞ and subscript $_L$ denotes longwave flux.

One problem with G^*_a is the lack of direct high-quality measurements at the surface on a global scale. Almost no measurements are available at the oceans. The present study explores how G_a and other correlative satellite data could be used to predict the surface longwave flux.

A comparative analysis of different approaches used in deriving the downward longwave flux is given next, followed by the theoretical formulation and a description of the input data sources. The present approach to obtain the surface fluxes from satellite measurements is described in the next section. The ocean and land surfaces have been treated separately. Validation of the parameterizations using data from field experiments is presented in Section 4. Section 5 describes application of the technique using ERBE (earth radiation budget experiment) and SSMI (special scanning microwave imager) water vapor data and illustrates how we can analyse the water vapor radiative interactions, followed by summary and discussions at the end.

2. Obtaining clear-sky downward surface flux from satellite measurements

2.1. Surface longwave radiation budget

There have been a number of studies dealing with the problem of retrieving the surface longwave radiation budgets. The methods employed can be classified as either physical, empirical or statistical. The physical methods are based on the application of the radiative transfer theory (Frouin et al., 1988; Darnell et al., 1983; Wu et al., 1989) employing the profiles of temperature, humidity and other species in the atmosphere. Random and systematic errors imposed on the retrieved geophysical parameters limit the accuracy of the surface longwave fluxes. For instance, sensitivity tests (Wu et al., 1989) have shown that an uncertainty of 2 K in temperature profile could cause an error of 5–6 W m^{-2} and an uncertainty of 10–20% in the relative humidity would result in errors of about 12 W m^{-2} in the surface flux. This explains why the standard errors in the surface fluxes derived from the operational satellites and even the full radiative transfer formalism are no

better than those derived from the empirical formulae. The numerous simple empirical relationships (Brutsaert, 1975; Idso, 1981; Schmetz et al., 1986; Tuzet, 1990) or bulk formulae employ the near-surface parameters to predict the downward flux. A drawback of these empirical methods is that they are applicable for only a selected range of surface temperatures and have very poor sensitivities to humidity perturbations in the atmosphere (Schmetz, 1986).

Statistical methods, on the other hand, employ a combination of top-of-the-atmosphere spectral radiances measured by AVHRR (advanced very high resolution radiometer) /HIRS-2-type (high resolution infrared sounder) instruments to obtain surface fluxes through regression techniques (Schmetz, 1986; Gupta, 1989). Gupta (1989) developed parameterized equations for computing the surface longwave flux based on the results of detailed radiative transfer computations using meteorological data from NOAA/TOVS (TIROS operational vertical sounder). Later the technique was modified (Gupta et al., 1992) using the meteorological data from the international satellite cloud climatology project (ISCCP) instead of TOVS. Employing a set of 330 soundings sampled from the global ISCCP-C1 (3 hourly data) dataset for July 1983, they report an rms error of 4.7 W m^{-2} between the parameterized model and the detailed radiative transfer calculations for clear skies.

A recent study (Stephens et al., 1994) using simulations of clear sky longwave fluxes to space and to the surface showed that the ratio of the two fluxes is a simple function of column water vapor. They employed the TOA ERBE broadband fluxes and SSMI water vapor data to derive the clear sky longwave radiative cooling rates in the atmosphere. The rms difference between the parameterization-retrieved surface fluxes and the simulated fluxes is about 6 W m^{-2}. The present study is similar in that we derive the surface flux from TOA flux, column water vapor and surface temperature. But the simulations use as input five years (1985–89) of ship sondes from pole to pole comprising more than 30 000 soundings. Further, the approach is more physically based and it explicitly resolves the window (8–12 μm). Why is it so critical to resolve the window? It will be shown later in the paper that it is essential to derive the radiative cooling in the window to infer water vapor feedback in the tropics (30° S to 30° N). For example, roughly 80% of the net IR cooling of the surface in the tropics occurs in the window. Furthermore, it is demonstrated that the window flux is critical for including the effects of non-black emission by land surfaces.

This study uses the cloud and the earth's radiant energy systems (CERES) satellite radiation budget instrument being developed for the NASA earth observing system (EOS). A brief description of CERES longwave measurements follows:

2.2. *CERES longwave measurements*

CERES employs a pair of broadband scanning radiometers which represent an improved version of the ERBE scanners. The radiometers have a total band (shortwave + longwave spanning 0.2 to 200 μm), a shortwave (0.2 to 4 μm) and a longwave window channel (8 to 12 μm). The broadband (4 to 200 μm) longwave flux is obtained from a combination of these channels. The spectral response characteristic of the longwave window channel is shown in Fig. 1.

Since the CERES instrument is not spaceborne yet, we demonstrate our method through model calculation of longwave fluxes (both broadband and window) at the TOA and at the surface. These calculations employ soundings deployed from ships. In an ideal situation, algorithms such as the present ones should be developed solely from observations of fluxes at TOA and at the surface.

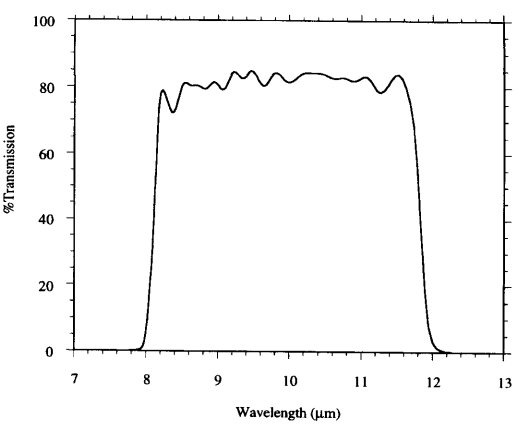

Fig. 1. Combined longwave filter transmission (average of both front and rear filters) for the CERES window channel (8–12 μm).

Such collocated observations are not available. The particular parameters used in our algorithm may need revision as observations become available.

2.3. *Model simulation and data*

The atmospheric greenhouse effect, G_a, along with other variables and parameters used in this study are defined in Table 1. The greenhouse effect and the downward flux density (G_a^*) at the surface can be expressed by employing the integral form of the solution to the equation of radiative transfer:

$$G_a = \int_0^\infty d\nu \int_{z_{top}}^0 A_\nu(z_{top}, z') \frac{dB_\nu(z')}{dz'} dz', \quad (1)$$

$$G_a^* = \int_0^\infty d\nu \left[B_\nu(z_{top}) A_\nu(z_{top}, 0) - \int_0^{z_{top}} A_\nu(0, z') \frac{dB_\nu(z')}{dz'} dz' \right], \quad (2)$$

where ν is the wavenumber in cm^{-1}, z is the altitude, $B_\nu(z')$ is the monochromatic Planck blackbody function corresponding to the temperature at level z', $A_\nu(z, z')$ is the monochromatic atmospheric absorptance, which is simply (1 — transmittance), between the levels specified in the arguments and z_{top} is the altitude at the top of atmosphere. A_ν is the absorption by water vapor, CO_2, ozone, CH_4, N_2O, trace gases and aerosols and it depends on the vertical distribution of temperature and the radiatively active species in the atmosphere. The transmittances have been computed using the $20\,cm^{-1}$ LOWTRAN 7 (Kneizys et al., 1988) transmittance code, and for the angular integration, we multiplied the absorber path length by the diffussivity factor of 1.66. However, the continuum model used in LOWTRAN 7 has been updated including a revised version (May 1994) of the Clough–Kneizys–Davies (CKD) model (Clough et al., 1980). Revisions effected in both the self and foreign continuum coefficients (Clough, 1995) to the data of Burch in the $1300\,cm^{-1}$ region have been validated against HIS (High Resolution Spectro-radiometer) spectra downlooking from 20 km and uplooking from the surface. Eqs. (1) and (2) are evaluated employing a quadrature scheme and a high vertical resolution equivalent to a vertical layer spacing ranging from a minimum of 1 mb to a maximum of 1/4 km. Agreement of the boundary fluxes using the ICCRM (Intercomparison of Radiation Codes in Climate Models) standard atmospheres (Ellingson, 1991) as input is within 2–3 $W\,m^{-2}$.

The input data used for this study consist of the ship rawinsondes for the years 1985–89 obtained from the National Center for Atmospheric Research (NCAR) data archive of NMC (National Meteorological Center) upper air data base. This time frame is chosen to coincide with the earth radiation budget observations (ERBE) for the same period. The locations of ship data over the entire globe used in this study is shown in Fig. 2. There is a fair distribution of data points to exclude any sampling-related problems in the analysis. The poor quality of humidity values above about 5–6 km, reported from soundings is well known (Elliot and Gaffen, 1991). An error analysis, employing the standard deviation of errors as reported by field tests of radiosonde instruments (Inamdar and Ramanathan, 1994), showed the error for the humidity mixing ratio to be distributed between 6% near the surface to nearly 13% at about 200 mb. Humidity data above 200 mb have not been used. To establish the fidelity of sonde data, an independent validation has been performed by employing the ERBE data. We use the daily clear-sky ERBE OLR data for 1985 extracted from the hour-box record in the same time window (within 24 hrs) and location as the ship data. The agreement between ERBE and model fluxes shown in a previous study (Inamdar and Ramanathan, 1994) is within the uncertainty limits of the ERBE instrument.

3. Parameterization

First the ship sondes were used as input in eqs. (1) and (2), to derive the TOA and surface longwave fluxes. We then fit the window and non-window components of downward flux in terms of the respective components of greenhouse effect as:

$$g^*_{a,win} = a_0 g_{a,win} + a_1, \quad (3)$$

$$g^*_{a,nw} = b_0 g_{a,nw} + b_1, \quad (4)$$

and next focus on seeking an optimum combination of parameters, P_i (Table 2), which best fit the deviations of the window and non-window fluxes

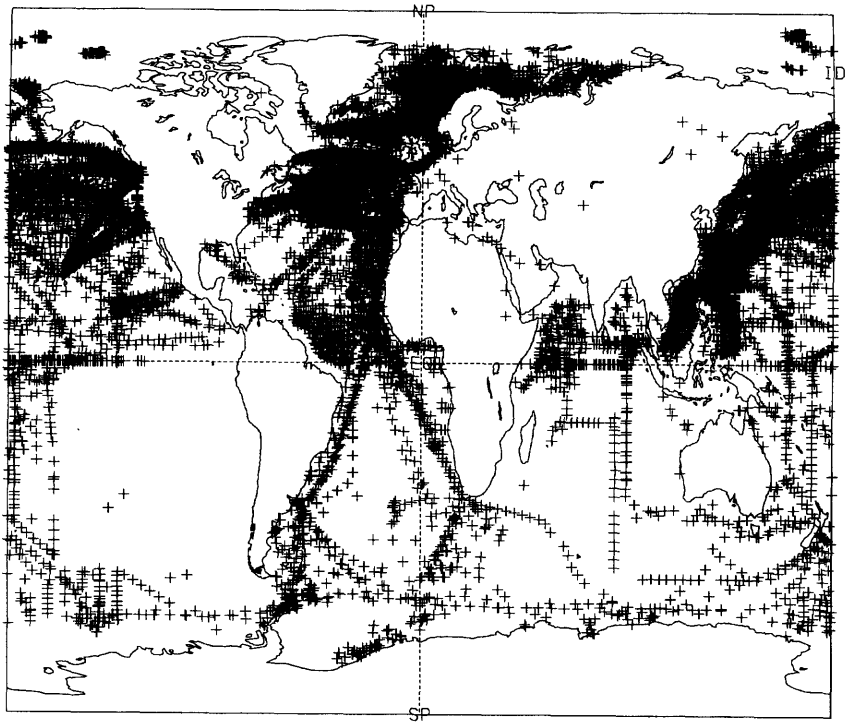

Fig. 2. Ship data locations (1985–89) over the global oceans used in this study.

as predicted from (3) and (4) above from the actual fluxes:

$$g^*_{a,win} - a_0 g_{a,win} = c_0 + f^+_{\infty,win} \sum_i c_i P_i, \quad (5)$$

$$g^*_{a,nw} - b_0 g_{a,nw} = d_0 + f^+_{\infty,nw} \sum_i d_i P_i, \quad (6)$$

where the a_i, b_i, c_i and d_i terms are constants to be determined through the regression analyses. The various terms in eqs. (3)–(6) are defined in Table 1. The atmospheric variables, P_i, have been chosen after a careful investigation of the physics of the problem and extensive sensitivity studies (described briefly below) to identify the parameters contributing most to the variability of the downward flux.

The physics of radiative transfer in the window and non-window spectral regions forms the basis of our algorithm. Eqs. (3) and (4) above are a result of the close correlation between the atmospheric greenhouse effect (G_a) and the downward emissions (Inamdar and Ramanathan, 1994) and also the unique relationships of the window and non-window components of G_a with SST and precipitable water (to be discussed below). Note that a two-step procedure is followed (the pair of eqs. (3), (5) and (4), (6)) in predicting each component of the downward flux. Although a single step regression could have yielded a similar or even better accuracy, this has been done to achieve a better physical consistency in the relationship between the TOA and surface fluxes.

We propose our standard model in terms of the window and the non-window components of g_a, $\ln(w_{tot})$, w_{tot}, $\ln(F^+_{\infty,win}/F^+_{0,win})$, T_s and T_a. All of the radiative flux parameters have been normalized with the surface blackbody emission to eliminate the surface temperature-dependence. Regression analysis of the radiative transfer-simulated fluxes has been performed separately for the tropics (30° S to 30° N) and extra tropics (30° to poles) to accomodate the different physics and thus achieve a better accuracy. Now, we will explain the physical basis of the parameterization.

For the non-window region, the variables, P_i, are (Table 2): $g_{a,nw}$, $\ln(w_{tot})$, T_s and T_a. As

explained earlier, the dependence of g_a^* on $g_{a,nw}$ follows from eqs. (1) and (2). So, it is not surprising, the surface flux is influenced by near surface parameters: T_s, T_a and w_{tot}. Note in this context that, the first 2 km contribute more than 70% to w_{tot}. Thus, w_{tot} is simply a surrogate for the boundary layer water vapor. Furthermore, the flux depends on ln w_{tot}, because the rotation and vibration-rotation bands of water vapor are in the logarthmic limit (Cess and Tiwari, 1972). The choice of 950 mb level for the near-surface air temperature is based on the optimum criteria from statistical considerations. In the opaque non-window spectral regions, the atmospheric absorption attains saturation close to the surface, and hence it is the near-surface emissions that determine the down flux. In fact more than 95% of the total downward flux originates in the first few kilometers. This is well illustrated in Fig. 3 which shows the relationships between the spectral distributions of greenhouse effect, surface emissions and the downward flux for a typical warm pool sounding. The curve for the down flux is seen to be almost inseparable from the surface blackbody curve except in the window and its immediate neighbourhood.

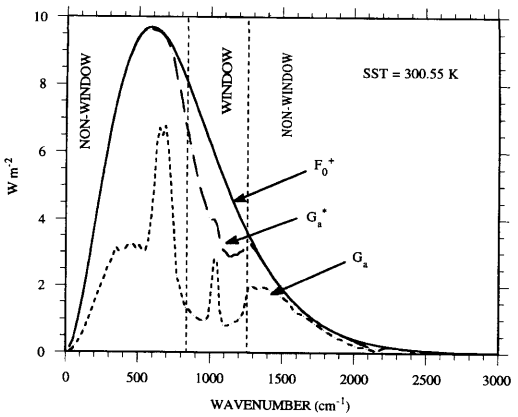

Fig. 3. Spectral distribution of surface blackbody emission, atmospheric greenhouse effect and downward flux at the surface highlighting the window spectral region for a typical warm pool sounding.

The variables, P_i, for the window region are (Table 2): $g_{a,win}$, w_{tot}, $\ln(F^+_{\infty,win}/F^+_{0,win})$, T_s and T_a. The atmospheric absorption in the window, in contrast to the non-window, does not attain saturation and is dominated by the water vapor continuum effect. Hence, it can be expressed as a combination of a linear limit and a temperature-dependence factor. Also, the window absorption is highly sensitive to the vertical distribution of moisture. The dynamic effects on water vapor and the exponential scaling of the total precipitable water with SST (Stephens, 1990) partly explain the superimposition of the non-linear effect in the window. The transmittance in the window being very nearly exponential, the ratio of window component of top-of-atmosphere to surface emissions yields an approximate measure of the optical depth.

Table 2. *Parameterization equations for oceans*

Model	Equation	Comments
tropics (30°S to 30°N) ocean	$g^*_{a,win} = 3.2504 g_{a,win} + [0.1377 w_{tot} + 3.46305 \ln(f^+_{\infty,win}/f^+_{0,win}) + 0.13866(T_s/300) + 1.12813(T_{950}/300)] f^+_{\infty,win} - 0.24155$	window rms error 3.3 W m^{-2}
	$g^*_{a,nw} = 0.25878 g_{a,nw} + [0.07363 \ln(w_{tot}) - 1.09875(T_s/300) + 1.442(T_{950}/300)] f^+_{\infty,nw} + 0.45445$	non-window rms error 1.7 Wm^{-2}
	$g^*_a = g^*_{a,win} + g^*_{a,nw}$	total rms error 4.4W m^{-2}
extra tropics (30° to Pole) ocean	$g^*_{a,win} = 1.6525 g_{a,win} + [0.15385 w_{tot} + 2.0074 \ln(f^+_{\infty,win}/f^+_{0,win}) - 0.29873(T_s/300) + 0.52062(T_{950}/300)] f^+_{\infty,win} - 0.01875$	window rms error 1.7 W m^{-2}
	$g^*_{a,nw} = 0.12284 g_{a,nw} + [0.07748 \ln(w_{tot}) - 1.52282(T_s/300) + 1.81629(T_{950}/300)] f^+_{\infty,nw} + 0.52066$	non-window rms error 2.0 W m^{-2}
	$g^*_a = g^*_{a,win} + g^*_{a,nw}$	total rms error 3.2 W m^{-2}

3.1. *Parameterization for ocean surfaces*

Table 2 and Figs. 4, 5 present a summary of the recommended models applicable over the open ocean. Inputs for the model are, in addition to the CERES broadband and window channel information, data on the surface and near surface (950 mb in this case) air temperature, and the total column precipitable water vapor, w_{tot} (g cm^{-2}) derived either through instruments such as the special sensor microwave imager (SSMI) measurements over the oceans, microwave sensors aboard the defence meteorological space program (DMSP) satellite or from detailed water vapor profiles derived from the TOVS data products. It is to be noted from Table 2 that the coefficients of $g_{a,win}$ and the window flux ratio term dominate in the tropics and explain the bulk of the variability. The combination of residual parameters of water vapor, temperature and window flux ratio appearing in square parenthesis are multiplied by the respective components of outgoing longwave flux to explain the non-linear variability in g_a at higher temperatures.

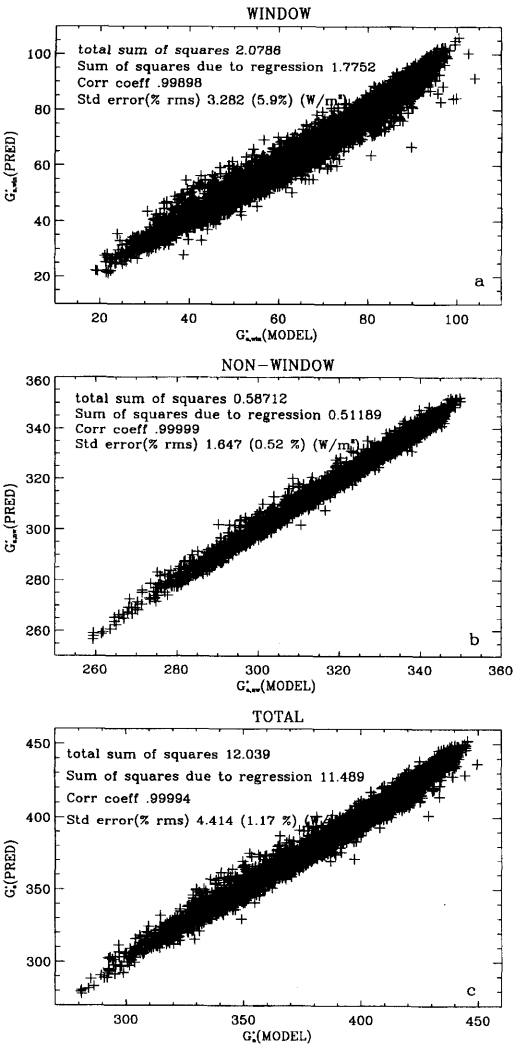

Fig. 4. Comparison of clear-sky downward longwave fluxes predicted from the parameterized model with those from the detailed radiative transfer calculations over the tropics (30° S to 30° N), for the (a) window, (b) non-window and (c) total longwave spectrum. The total number of data points used is $n=5816$.

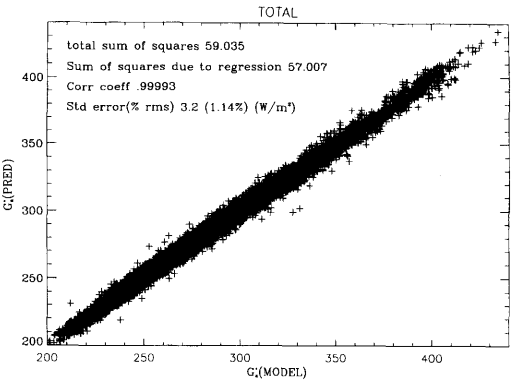

Fig. 5. Same as in Fig. 4c, but for the extra tropics (30° to poles). $n=23096$.

The standard error between the radiative fluxes derived from the full radiative transfer model (G_a^* (model) in Fig. 4c) and that predicted by the parameterization (G_a^* (pred)), is about $\sim$4.4 W m^{-2} for the tropics and 3.2 W m^{-2} for the extra-tropics (Fig. 5). The terms "total sum of squares", $\Sigma[g_a^*(\text{model})-\bar{g}_a^*]^2$; "sum of squares due to regression", $\Sigma[g_a^*(\text{pred})-\bar{g}_a^*]^2$, where $\bar{g}_a^*$ is a mean value of g_a^* (model); and correlation coefficient shown in Figs. 4, 5 represent statistical measures of the goodness of fit. A comparison of the former two terms reveals how closely the chosen parameters explain the total variance of the predicted quantity. The correlation between the model and predicted fluxes is very high (0.9998) and the regression line is extremely close to the 45° line indicating absence of any bias in the parameterized flux estimates.

3.2. *Parameterization for land surfaces*

The same technique described in the previous sub-section can be applied for non-black surfaces. The formulation for the upwelling flux at any level z with a non-black emitting underlying surface with emissivity ε can be expressed as:

$$F_z^+(J) = B_J(z) - \int_0^z \mathrm{Tr}_J(z, z') \frac{\mathrm{d}B_J(z')}{\mathrm{d}z'} \mathrm{d}z'$$
$$-(1-\varepsilon_J)B_J(0)Tr_J(0, z)$$
$$+(1-\varepsilon_J)\mathrm{Tr}_J(0, z)G_a^*(J),$$

where for the sake of simplicity, the summation over wavenumber v has not been shown. J is the band with: $J=1$ for the non-window region and $J=2$ for the window region. The term Tr denotes the atmospheric transmittance between the altitude levels specified in the arguments. The first three terms on the right-hand side represent the regular two-stream solution with modification for a non-black emitting underlying surface, while the last term denotes enhancement due to reflection of the atmospheric emission to the ground.

As shown in Fig. 3, $G_a^*(J) \approx B_J(0)$ for the non-window region. As a result, the last two terms on the right nearly cancel each other and the non-black emission has a negligible effect on F_∞^+. However, for the window region, particularly in the extra-tropics, $G_a^*(J) \ll B_J(0)$, and non-black emissions become important.

A detailed spectral data for the surface emissivity as a function of various land surface types is unavailable. However, a global emissivity map for the 8 to 10 μm region has been obtained by Prabhakara and Dalu (1976). The source of emissivity data is the infrared spectral measurements made by the Nimbus 4 infrared interferometer spectrometer (IRIS). The sandy desert regions have been found to be characterized by low emissivities (~0.7), essentially resembling the emissivity due to quartz and the emissivity approaches unity for moist and vegetative surfaces. Furthermore, it is suggested that the window emissivity is substantially non-black, while the non-window regions may be closer to being black. Here we consider 2 cases.

(1) The Prabhakara and Dalu's emissivity data in the 8–10 μm region is applicable in the entire longwave spectrum, i.e., $\varepsilon(\mathrm{nw}) = \varepsilon(\mathrm{window}) = \varepsilon(8\text{–}10\ \mu\mathrm{m})$.

(2) The non-window region is black, i.e., $\varepsilon(\mathrm{nw}) = 1.0$ and $\varepsilon(\mathrm{window}) = \varepsilon$ (8 to 10 μm).

NMC upper air data for 1985 Jan and July are used as model input for the atmosphere.

Application of the parameterization approach outlined earlier is shown in Fig. 6 for case 1 above, where the rms error in the predicted fluxes is 6 W m^{-2}. Table 3 shows the coefficients for both cases. An interesting aspect of the present parameterization is the critical importance of the window channel measurement. For example, without the window channel radiance, the error for case 1 doubles to 12 W m^{-2} (Fig. 7).

4. Validation

The data sources used in the validation exercise come from the central equatorial pacific experiment (CEPEX) conducted in March/April 1993 which was a multi-platform endeavour.

The research vessel Vickers, with a cruise track along the equator starting from Honiara (160° E, 10° S) to Christmas islands (160° W, 5° N), made state-of-the-art measurements of temperature, humidity and ozone mixing ratios between 8 and 21 March, 1993. The ship also had aboard a Fourier Transform Infrared Spectroradiometer (FTIR) measuring the narrow field of view (Lubin, 1994) incoming longwave radiance in the 5–20 μm region, and in addition an Eppley pyrgeometer to measure the broadband longwave fluxes. The

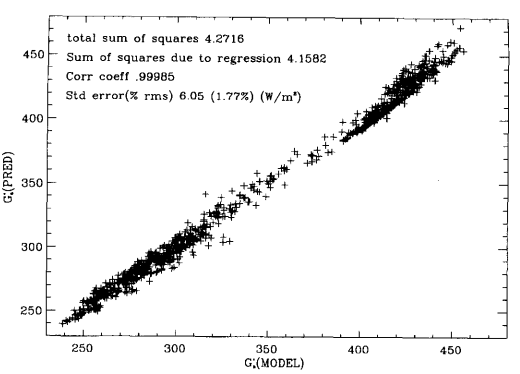

Fig. 6. Comparison of the fluxes predicted by the parameterization (Table 3) with the model for land surfaces including the effect of surface emissivity for case 1 (i.e., a non-black surface in both the window and non-window).

Table 3. *Parametererization equations for land for the tropics only (30° S to 30° N). Parameterization was not attempted for the extra-tropics due to lack of emissivity data*

Model	Equation	Comments
*Case 1: $\varepsilon(\text{nw})=\varepsilon(\text{win})=\varepsilon(8\text{–}12\ \mu\text{m})$	$g^*_{a,win}=2.6054g_{a,win}+[0.1372w_{tot}+2.1209\ln[f^+_{\infty,win}/(\varepsilon f^+_{0,win})]+0.04031(T_s/300)+0.11253(T_{950}/300)]f^+_{\infty,win}-0.0081$	window rms error 4.5 W m^{-2}
	$g^*_{a,nw}=0.2541g_{a,nw}+[0.05878\ln(w_{tot})-2.0534(T_s/300)+2.46958(T_{950}/300)]f^+_{\infty,nw}+0.45018$	non-window rms error 2.7 W m^{-2}
	$g^*_a=g^*_{a,win}+g^*_{a,nw}$	total rms error 6 W m^{-2}
†Case 2: $\varepsilon(\text{nw})=1$; $\varepsilon(\text{win})=\varepsilon(8\text{–}12\ \mu\text{m})$	$g^*_{a,nw}=0.199g_{a,nw}+[0.09949\ln(w_{tot})-1.26611(T_s/300)+1.7713(T_{950}/300)]f^+_{\infty,nw}+0.40193$	non-window rms error 3.3 W m^{-2}
	$g^*_a=g^*_{a,win}+g^*_{a,nw}$	total rms error 6.2 W m^{-2}

* Please note that the surface emission-related terms $g_{a,win}$ and $g_{a,nw}$ are corrected for surface emissivity. That is, $g_{a,win}=\varepsilon F^+_{0,win}-F^+_{\infty,win}$ and $g_{a,nw}=\varepsilon F^+_{0,nw}-F^+_{\infty,nw}$.
† Equation for the window component is identical to case 1.

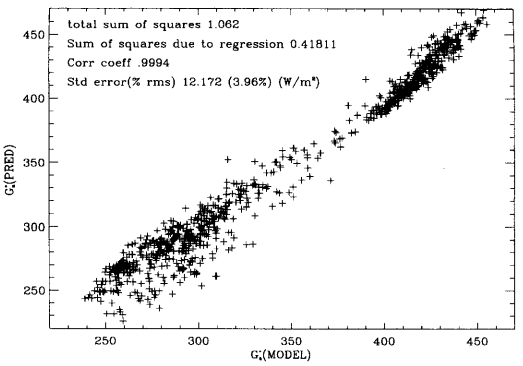

Fig. 7. Same as Fig. 6, but using only the broadband components of flux (simulated from the theoretical model). Comparison with Fig. 6 suggests the effectiveness of window channel in capturing the variability due to a non-black surface.

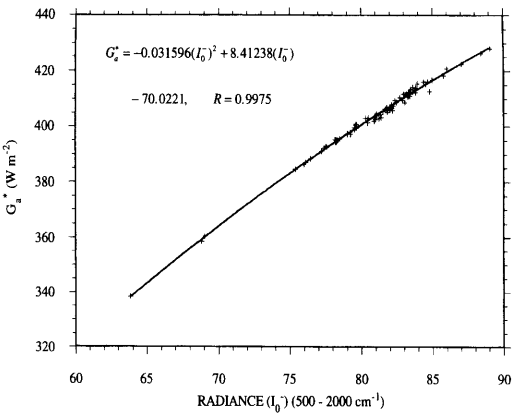

Fig. 8. Radiative transfer model-simulated broadband fluxes and radiances for the FTIR spectral range of 5 to 20 μm for the Vickers sondes. The equation inset in the figure shows the quadratic fit employed to derive the FTIR fluxes.

FTIR radiances are converted to broadband fluxes using the following procedure: Vickers soundings are used as input and eq. (2) is used to simulate both the broadband longwave fluxes and the 5 to 20 μm radiances under clear skies. A plot of these (Fig. 8) indicated an excellent quadratic fit with a correlation coefficient of 0.999. The broad band fluxes derived from this relation are referred to as "FTIR fluxes" and form the basis of our comparison. The comparison is restricted to the days identified as "clear skies" made by visual observations of overhead sky conditions aboard the ship.

Temperature and total precipitable water obtained from the Vickers sondes, and TOA fluxes simulated from the radiative transfer model have been input into eqs. (3)–(6). Fluxes thus estimated from the parameterization are shown in Fig. 9a. Fig. 9b shows the FTIR-measured radiances

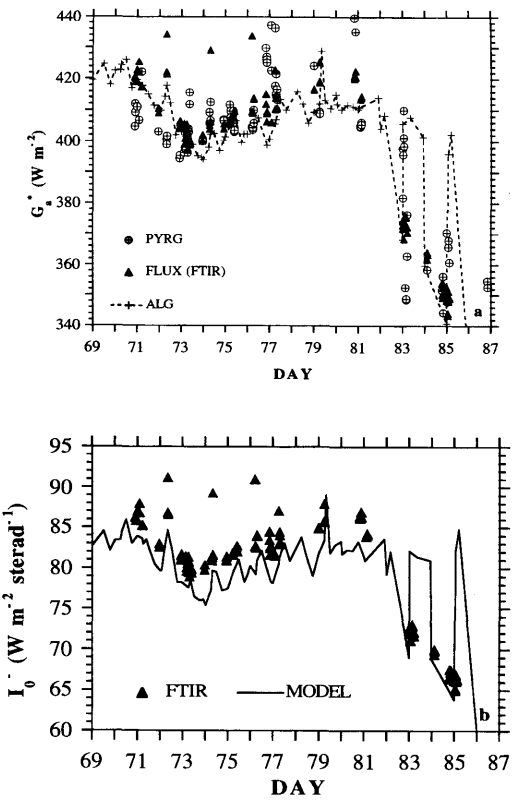

Fig. 9. (a) Comparison of longwave fluxes predicted by the parameterization (marked ALG on the Figure) with FTIR and Eppley Pyrgeometer (marked as PYRG) measurements aboard the R/V Vickers between Mar 11 and Mar 22, 1993. (b) The FTIR-measured radiances integrated between 5 and 20 μm, compared with those computed by the radiative transfer model for the same spectral range.

against the detailed radiative transfer model derived radiances integrated between the FTIR spectral range of 5 to 20 μm. It must be borne in mind that the observed sky conditions referred to the FTIR instrument field-of-view only. The presence of clouds is apparent, as indicated by sharply higher values measured by the Eppley pyrgeometer (especially on day 77). A few of the FTIR observations also between day 72 and day 76 are significantly higher, and are apparently cloud-contaminated. This could be due to the presence of thin cirrus, which is difficult to detect or invisible trade cumulus overhead. Despite these shortcomings, the agreement of the parameterization estimates of fluxes is good with those of the FTIR and Pyrgeometer measurements (Fig. 9a). The model radiances (Fig. 9b) seem to be systematically lower than the FTIR. Further the FTIR fluxes are even higher than the Pyrgeometer for days 70–74 (Fig. 9a) is surprising, suggesting a calibration-related uncertainty in either or both instruments of nearly 5–8 W m^{-2} and possible errors in the method used to convert the FTIR radiances to fluxes (Fig. 8).

One must be careful in attempting to evaluate and judge the rms accuracy of the parameterization with respect to measurements based on the comparisons shown in Fig. 9. First we do not have a statistically large number of samples. Secondly, one must also bear in mind the contamination of at least some of the samples with cloud as apparent from Fig. 9. And thirdly, the calibration uncertainties of the instruments demonstrated above mask the real accuracy.

5. On inferring water vapor — radiative interactions

Lastly, we illustrate how the technique developed here can be used to understand the link between water vapor variations and the atmospheric greenhouse effect. We consider seasonal, latitudinal and inter-annual variations. All of these examples illustrate the fundamental importance of estimating G_a and G_a^* for the window region.

5.1. *Seasonal variations in G_a, G_a^* and radiative cooling*

We use ERBE data for the period 1985–89. However, since the ERBE scanner does not have a window channel, we employ a simplified form of the parameterization, referred to as the "ERBE-like" fit hereafter, which has been developed following the same approach as outlined in Section 3, eqs. (3)–(6), but using only the broadband component of flux. Analogous to eqs. (3)–(6), we can write,

$$g_a^* = a_0 g_a + a_1, \tag{7}$$

and express

$$g_a^* - a_0 g_a = b_0 + f_\infty^+ \sum_i b_i P_i \tag{8}$$

where the a_i and b_i terms are constants as before, and the parameters P_i, here comprise only the

total column water vapor (in the form of linear and logarthmic terms in eq. (8)) and the surface temperature. The former is obtained from the SSMI measurements and interpolated to the same grid size ($2.5 \times 2.5°$) as ERBE, while the surface temperatures are taken from the NMC-blended analysis of Reynold's (1988). Fig. 10 shows seasonal variation of G_a and down flux from both ERBE and model calculations for all the oceans (0–25° N). We chose only the northern hemisphere, because of the reduced number of ship samples south of the equator. Comparison of fluxes derived from the detailed radiative transfer model with ERBE measurements will pose a difficulty because of the sampling of the ship data locations. To overcome this problem, model results are first binned in intervals of 0.25 K SST and 0.2 g cm^{-2} precipitable water in the form of a look-up table. Numbers picked from this table corresponding to the NMC-blended SST and SSM/I water vapor form the curve labelled as "model" in Fig. 10.

There is a consistent, but very small bias of less than about 5 W m^{-2} (Fig. 10) in the ERBE (Kiehl and Briegleb, 1991; Collins and Inamdar, 1995), which is well within the ERBE instrument uncertainties. Interestingly, this bias almost disappears for the surface longwave flux (see bottom panel of Fig. 10), demonstrating the advantage of the present two-step approach to the parameterization. This has an important benefit in dealing with the scene id problems whereby errors in the TOA satellite-measured fluxes do not propagate to the surface.

Fig. 10 illustrates several important features.(i) There is a large seasonal variation (about 16 W m^{-2} peak to peak) in the atmospheric greenhouse effect, due to a correspondingly large seasonal variation in the surface temperature and column water vapor (Fig. 11); The increase in water vapor from winter to summer is in part due to the northward migration of the ITCZ and partly due to the increase in frequency of deep convection with SST. (ii) The increase in G_a^* (see bottom panel) is even larger (≈ 25 W m^{-2} peak to peak) such that the atmospheric cooling (Fig. 12) increases with water vapor and surface temperature; (iii) The increase in surface-atmosphere column greenhouse forcing (G_a) and the surface greenhouse forcing (G_a^*) are comparable to about a third of the increase in the seasonal solar radiative heating. The fundamental inferences from Figs. 10 to 12 are two-fold: First, seasonal variation in the water vapor greenhouse forcing is an important component of the radiat-

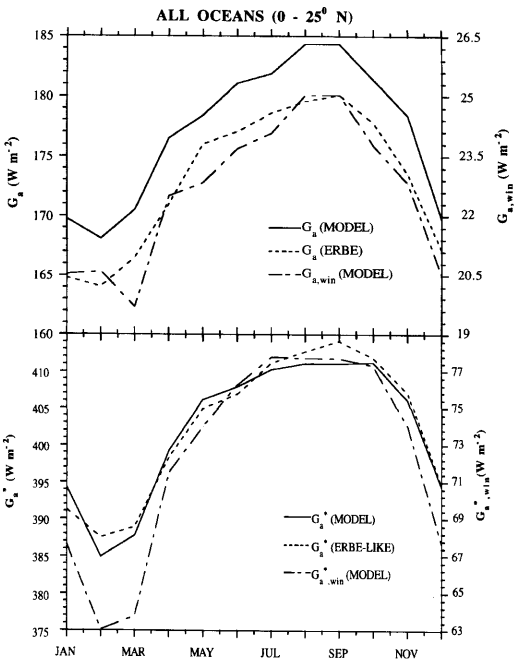

Fig. 10. Seasonal variability of atmospheric greenhouse effect (top) and surface flux (bottom) derived from ERBE and the ERBE-like algorithm. The model results and corresponding window components are also shown. The ERBE-like fluxes shown in the bottom panel have been derived by using the NMC SST, SSM/I H2O and the ERBE broadband flux in eqs. (7)–(8).

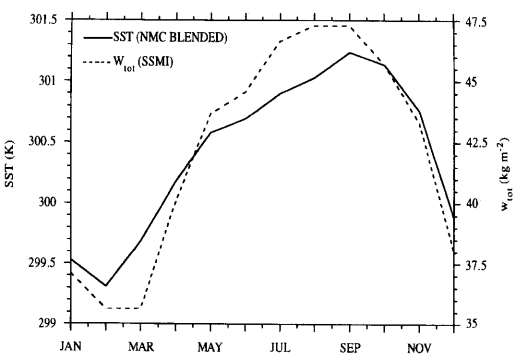

Fig. 11. Variability of SST and total precipitable water that were used to obtain results depicted in Fig. 10.

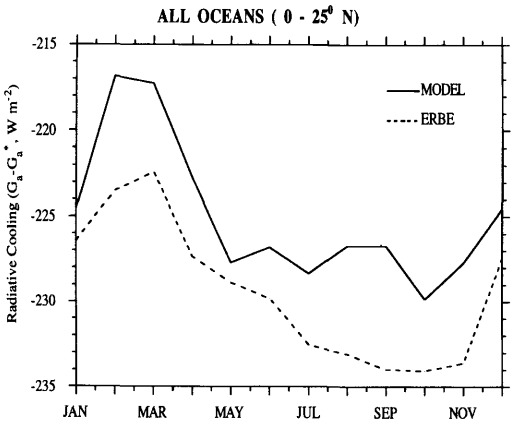

Fig. 12. Seasonal variabilty of atmospheric column longwave radiative cooling for all the oceans between 0 and 25° N, derived from both the model and ship sondes (solid line) and collocated ERBE data in conjunction with the ERBE-like parameterization (dashed line).

ive-dynamical feedbacks that govern the tropical seasonal climate. And secondly, the variations are so large that they constitute a critical test for model simulations of the water vapor–radiative interactions in the tropics.

Water vapor continuum plays an important role, not only in the seasonal variation, but also in the latitudinal gradient (Fig. 13). It is just as important as the non-window region in determining the latitudinal gradient in the atmospheric LW radiative heating (top panel of Fig. 13) and is the dominant source of the net surface LW radiative cooling in the tropics (bottom panel of Fig. 13). For example, at the equator, the window cooling at the surface is about 40 W m^{-2}, while the non-window cooling is only 10 W m^{-2}.

5.2. *Interannual Variations*

Estimates of the interannual variations are not only relevant for understanding the processes governing natural variability but are also very critical for validating the coupled ocean-atmosphere models. In Fig. 14, we present the time series of changes in surface emission (ΔF^+), atmospheric greenhouse effect (ΔG_a) and downward surface flux (ΔG_a^*) for the period July 87 to December 89 for the entire tropical pacific (30° N to 30° S). The changes refer to the month of Febuary 89 when the lowest average SST was recorded. The data

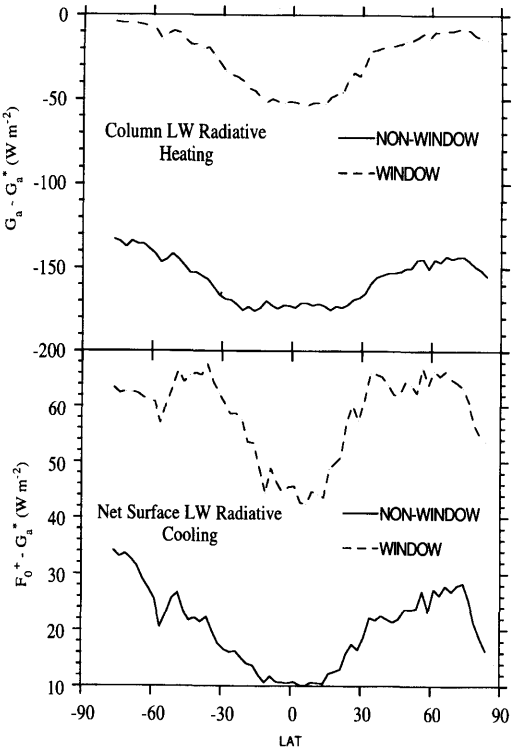

Fig. 13. Latitudinal distribution of atmospheric column longwave radiative heating (top panel) and net surface longwave radiative cooling (bottom panel) resolved into the window and non-window components.

set was produced by applying the ERBE-like fit (eqs. (7) and (8)) to ERBE and SSMI water vapor data as described above, and then averaged between 30° N and 30° S with latitudinal weighting.

There are several similarities between the greenhouse forcing changes found for the case of the seasonal variations in the northern tropical oceans (Fig. 10) and inter-annual variations for the entire tropics (Fig. 14). First, there is a strong positive correlation between surface temperature, water vapor amount, G_a and G_a^*. Secondly, the variations in G_a^* far exceed those in the black body surface emission. Thus in the warmer-humid atmosphere, the column greenhouse effect is larger; the surface radiative heating is even larger such that the atmospheric LW radiative cooling increases in the warmer atmosphere.

The role of continuum absorption by water vapor in the atmospheric window (8–12 μm) is

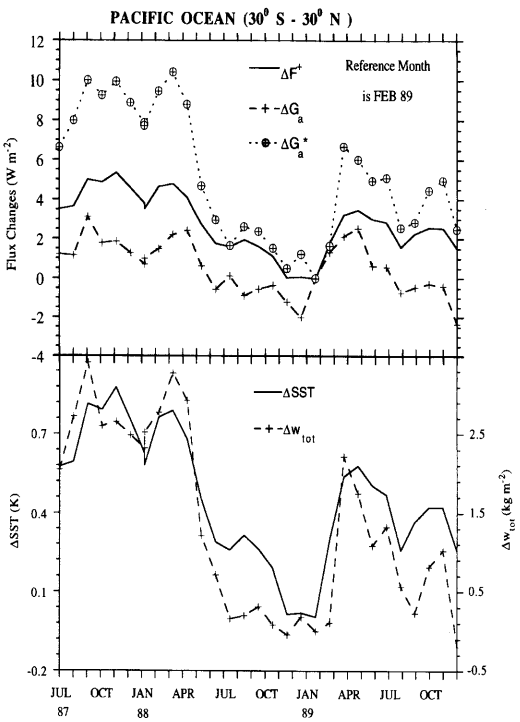

Fig. 14. Time series of changes in F^+, G_a and G_a^* for the Pacific ocean (top) between 87 July and 89 Dec. The change refers to the month of Feb 89 which corresponds to the lowest SST. The corresponding changes in SST and total water vapor are shown at the bottom.

investigated by examining the changes in G_a, G_a^* and radiative cooling between the JJA (June–July–August) and DJF (December–January–February) seasons for the northern hemisphere oceans (Fig. 15). It is evident that window accounts for a major fraction of the change in the surface flux. Interestingly, the atmospheric LW radiative cooling (represented in Fig. 15 by the ΔR terms) in the window exceeds the total, while there is a slight heating of the tropospheric column in the non-window spectral regions.

6. Summary and discussion

The present work represents an extension of the principles outlined in our earlier paper (Inamdar and Ramanathan, 1994) and demonstrates how to exploit the potential of TOA measurements in the window (8–12 μm) and broadband flux from the next generation of satellite instruments (CERES) for gaining new insights into the physics of greenhouse effect and water vapor radiative interactions.

The physically-based formulation illustrates how to utilize the TOA window and non-window spectral fluxes to obtain the surface fluxes. The algorithm employs the CERES broadband and window TOA flux measurements, the surface temperature, the near-surface atmospheric temperature and the total column water vapor content of the atmosphere.

Owing to the close affinity of the downward flux with the column greenhouse effect, the downward emissions in the window and non-window are first constrained in terms of their respective components of greenhouse effect, and in the second step the deviation of the predicted flux is explained in terms of the other residual variables. This approach handles errors in scene identification and in the TOA fluxes very well. The tropical (30° S to 30° N) and extra tropical (30° to poles) oceans and land surfaces have been treated separately owing to the differences in the physics and to achieve the best accuracy. The rms accuracies obtained range between 3–6 W m^{-2} and the correlation coefficient between the model-simulated fluxes and that predicted by the parameterization has been found to be extremely good (0.999). The critical importance of the window channel for non-black surfaces has been demonstrated.

Validation studies employing data from the CEPEX indicate a reasonable agreement between the measurements and the parameterized flux estimates. The agreement is within the limits of uncertainties posed by the errors in scene identification, instrument calibration and/or aerosol emissions in the lower atmosphere. Our scheme does not allow for the aerosol effects. Sensitivity studies (not reported here) have revealed that thick haze in the atmospheric boundary layer (horizontal visibilities <15 km) could enhance the downward emissions by about ~ 3–5 W m^{-2}. Measurements at the ARM sites at Oklahoma and Kavieng also support this fact. While there have been few, if any, simultaneous measurements of aerosols and longwave fluxes in the atmosphere to validate, a proposal to add an additional parameter in the form of aerosol visible optical depth in future is under consideration.

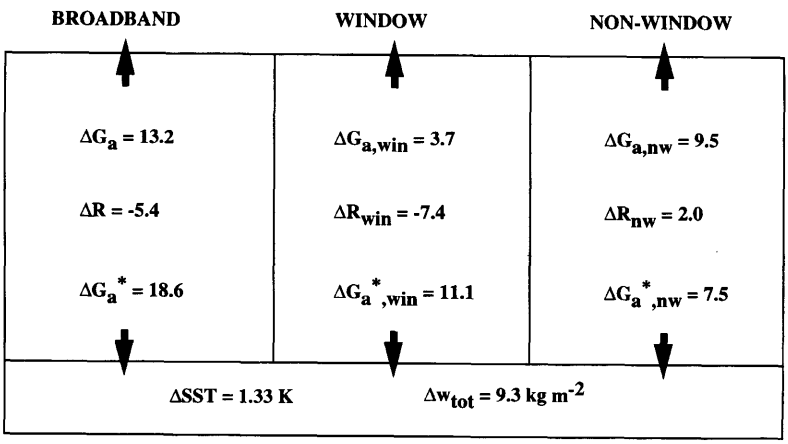

Fig. 15. Changes in the atmospheric greenhouse effect (ΔG_a), surface flux (ΔG_a^*) and atmospheric column radiative cooling (ΔR) between the JJA and DJF seasons for all oceans (0–25° N). The respective window and non-window components of the changes are shown in the center and right panels.

Finally, application of the techniques has been illustrated by employing the ERBE data in conjunction with the SSMI-derived total precipitable water in assessing the water vapor radiative interactions. The time series of changes in the surface emission, atmospheric greenhouse forcing and the downward flux follow a seasonal pattern indicating increased radiative cooling of the atmosphere at higher SSTs and higher water vapor content. The effect of these changes on the globally-averaged OLR and in particular the relative roles of different parts of the troposphere on the OLR have an important bearing on the global-scale water vapor feedback. This is where the CERES instrument with its window channel will be able to resolve such changes due to temperature and water vapor.

Consider for example the fundamental deduction from Figs. 14, 15. The surface-atmosphere column greenhouse forcing for the warmer-humid tropical atmosphere is larger ($\Delta G_a > 0$). But, the increase in surface forcing is even larger and exceeds the increase dictated by the black body emission, i.e., $\Delta G_a^* \gg \Delta G_a$. As a result, tropospheric radiative cooling increases significantly with a warming. How would the system equilibrate? The system considered in Fig. 15 is an open system for which dynamical heat fluxes in the atmosphere and the ocean can easily restore the balance. But, if the global averaged G_a and G_a^* exhibit the same behaviour shown in Figs. 14 and 15, the increase in the radiative cooling of the troposphere must be balanced by an increase in the latent heating or an increase in the atmospheric solar heating (due to an increase in cloudiness). Simultaneous global observations of cloud radiative forcing at the TOA (CERES will provide this) and at the surface (CERES hopes to provide this through indirect techniques such as those presented here) in conjunction with evaporation data will close this fundamental gap in our knowledge of the climate system.

7. Acknowledgements

This work was supported by grants under the NASA–CERES project. We thank the two anonymous reviewers who helped us to improve the clarity of the presentation.

REFERENCES

Brutsaert, W. 1975. On a derivable formula for longwave radiation from clear skies. *Water Resources Research* **11**, 742–744.

Cess, R. D. and Tiwari, S. N. 1972. Infrared radiative energy transfer in gases. In: *Adv. Heat Transfer* **8**, Academic Press (New York), pp. 229–250.

Clough, S. A., Kneizys, F. X., Davies, R. W., Gamache, R. and Tipping, R. H. 1980. Theoretical line shape for

water vapor; application to the continuum. In: *Atmospheric water vapor*, edited by A. Deepak, T. D. Wilkerson and L. H. Rhunke. Academic Press, pp. 25–46.

Clough, S. A. 1995. The water vapor continuum and its role in remote sensing. In: *Optical remote sensing of the atmosphere*, vol. 2, 1995 OSA Technical Digest Series. (Optical Society of America, Washington, DC, 1995), pp. 76–78.

Collins, W. D. and Inamdar, A. K. 1995. Validation of clear-sky fluxes for tropical oceans from the earth radiation budget experiment. *J. Climate*, **3**, 569–578.

Darnell, W. L., Gupta, S. K. and Staylor, W. F. 1983. Downward longwave radiation at the surface from satellite measurements. *J. Climate Appl. Meteor.* **22**, 1956–1960.

Dutton, J. A. 1995. An analytical model of atmospheric feedback and global temperature change. *J. Climate* **8**, 1122–1139.

Ellingson, R. G., Ellis J. S. and Fels, S. B. 1991. The intercomparison of radiation codes used in climate models: longwave results. *J. Geophys. Res.* **96**, 8929–8953.

Elliot, W. P. and Gaffen, D. J. 1991. On the utility of radiosonde humidity archives for climate studies. *Bull. Amer. Meteor. Soc.* **72**, 1507–1520.

Frouin, R., Gautier, C. and Morcrette, J. J. 1988. Downward longwave irradiance at the ocean surface from satellite data: Methodology and in situ validation. *J. Geophys. Res.* **93**, C1, 597–619.

Gupta, S. K. 1989. A parameterization for longwave surface radiation from Sun-synchronous satellite data. *J. Climate* **2**, 305–320.

Gupta, S. K., Darnell, W. L. and Wilber, A. C. 1992. A parameterization for longwave surface radiation from satellite data: recent improvements. *J. Appl. Meteor.* **31**, 1361–1367.

Idso, S. B. 1981. On the systematic nature of diurnal patterns of differences between calculations and measurements of clear sky atmospheric thermal radiation. *Quart. J. Roy. Meteor. Soc.* **107**, 737–741.

Inamdar, A. K. and Ramanathan, V. 1994. Physics of greenhouse effect and convection in warm oceans. *J. Climate* **7**, 715–731.

Kiehl, J. T. and Briegleb, B. 1992. Comparison of the observed and calculated clear sky greenhouse effect: implications for climate studies. *J. Geophys. Res.* **97**, 10037–10049.

Kneizys, F. X., Shettle, E. P., Abreu, L. W., Chetwynd, J. H., Anderson, G. P., Gallery, W. O., Selby, J. E. A. and Clough, A. A. 1988. *Users Guide to Lowtran 7*. Rep. AFGL-TR-88-0177, Air Force Geophysics Lab., 137 pp.

Lubin, D. 1994. The rôle of the tropical super greenhouse effect in heating the ocean surface. *Science* **265**, 224–227.

Minschwaner, K. and McElroy, M. B. 1992. A model for the energy budget of the atmosphere — comparison with data from the earth radiation budget experiment. *Planetary and Space Science* **40**, 1237–1250.

Prabhakara, C. and Dalu, G. 1976. Remote sensing of the earth's surface emissivity at 9 μm over the globe. *J. Geophys. Res.* **21**, 3719–3724.

Raval, A. and Ramanthan, V. 1989. Observational determination of the greenhouse effect. *Nature* **342**, 758–761.

Reynolds, R. W. 1988. A real-time global sea surface temperature analysis. *J. Climate* **1**, 75–86.

Schmetz, P., Schmetz, J. and Raschke, E. 1986. Estimation of daytime downward longwave radiation at the surface from satellite and grid point data. *Theor. Appl. Climatol.* **37**, 136–149.

Stephens, G. L. 1990. On the relationship between water vapor over the oceans and sea surface temperature. *J. Climate*, **3**, 634–645.

Stephens, G. L. and Greenwald, T. J. 1991. The earth's radiation budget and its relation to atmospheric hydrology (1). Observations of the clear sky greenhouse effect. *J. Geophys. Res.* **96**, 15311–15324.

Stephens, G. L., Slingo, A., Webb, M. J., Minnett, P. J., Daum, P. H., Kleinman, L., Wittmeyer, I. and Randall, D. A. 1994. Observations of the earth's radiation budget in relation to atmospheric hydrology (4). Atmospheric column radiative cooling over the world's oceans. *J. Geophys. Res.* **99**, 18585–18604.

Tuzet, A. 1990. A simple method for estimating downward longwave radiation from surface and satellite data by clear sky. *Int. J. Remote Sensing* **11**, 125–131.

Wu, M. C. and Cheng, C. P. 1989. Surface downward flux computed by using geophysical parameters derived from HIRS 2/MSU soundings. *Theor. Appl. Climatol.* **40**, 37–51.